PHASE SPACE APPROACH TO SOLVING THE SCHRÖDINGER EQUATION: THINKING INSIDE THE BOX

DAVID J. TANNOR, NORIO TAKEMOTO, and ASAF SHIMSHOVITZ

Department of Chemical Physics, Weizmann Institute of Science, Rehovot, 76100 Israel

COPYRIGHTED MATERIAL

CONTENTS

I. INTRODUCTION

In 1946, Gabor proposed using a set of Gaussians located on a time–frequency lattice as a basis for representing arbitrary signals [1]. Gabor's motivation can be understood by considering Fig. 1a. If one considers an acoustical signal, generally

Advances in Chemical Physics, Volume 156, First Edition. Edited by Stuart A. Rice and Aaron R. Dinner.
© 2015 John Wiley & Sons, Inc. Published 2015 by John Wiley & Sons, Inc.

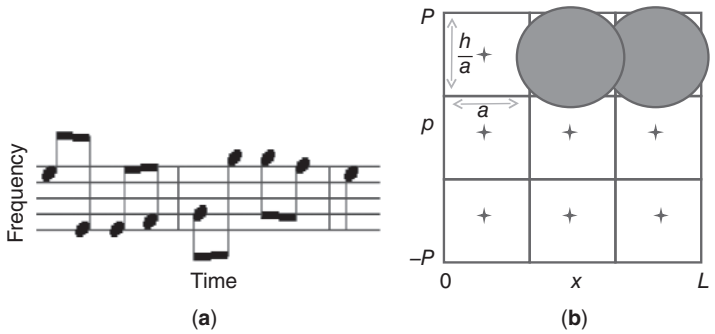

Figure 1. (**a**) A section of Beethoven's fifth symphony, showing that if a musical score is viewed as a plot of the time–frequency plane there is strong correlation between frequency and time. Note that most of the time–frequency phase space cells are empty. (**b**) A schematic representation of the von Neumann lattice in which one Gaussian is placed in every phase space cell of area h. For a color version of this figure, see the color plate section.

there is some form of time–frequency correlation. This is made explicit in musical notation, where the score can be thought of as a two-dimensional (2D) time–frequency plot, showing schematically that not all frequencies are present at all times. Gabor's proposal was to divide this 2D time–frequency space into cells of area 2π and place one Gaussian per cell. If the Gaussians are considered as a basis set, intuitively a substantial fraction of the Gaussians may be expected to have near-vanishing coefficients.

It turns out that the identical lattice of Gaussians was discovered by von Neumann 15 years earlier in the context of quantum mechanics, where instead of ω and t the conjugate variables are p and x and the area of the unit cell is h [2]. However, in all respects the formalism is isomorphic. Von Neumann's interest was in a generalized uncertainty principle, but subsequently mathematical physicists explored the properties of the von Neumann lattice as a basis. It was proven that if one Gaussian is placed per cell of area h the von Neumann basis is complete but not overcomplete, provided the width parameter of the Gaussian is appropriate to the cell size [3]. In the late 1970s, Davis and Heller [4] explored the use of the vN basis for solving the time-independent Schrödinger equation (TISE). Their motivation was similar to that of Gabor's. They reasoned that the classical mechanical phase space contour at energy E should provide an excellent guide for where quantum mechanical basis functions are needed. To the extent that basis functions outside the classical contour can be eliminated, the basis should provide a very efficient representation. Some prototypical examples of classical energy contours are illustrated in Fig. 2.

Although the commercial aspects of the representation are probably much larger for audio and image processing than for quantum mechanics, the advantage of the von Neumann representation is potentially much higher in quantum

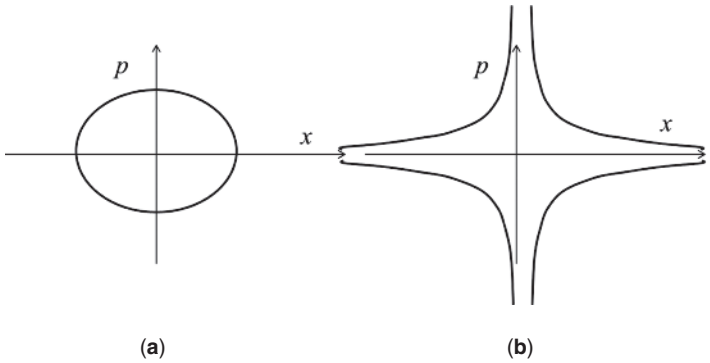

Figure 2. Classical phase space contours for (**a**) harmonic oscillator Hamiltonian, (**b**) Coulomb Hamiltonian.

mechanics. The reason is that quantum mechanical calculations for realistic atoms and molecules involve solving a wave equation in $3N$ degrees of freedom, where N is the number of electrons and nuclei, a dimensionality much higher than one deals with in signal and image processing. Most basis function methods use a tensor product Hilbert space and as a result the number of basis functions grows exponentially with the number of degrees of freedom. This notorious problem is called the "exponential wall" [5]. Although the von Neumann basis functions in multidimensions are direct products of one-dimensional (1D) Gaussians, the Hilbert space after removing the energetically inaccessible Gaussians is *not* a tensor product Hilbert space. Thus, formally at least, the method has the potential to defeat the exponential wall in basis set calculations.

Due to its intuitive appeal and its potential for simple and efficient representation, the von Neumann representation has attracted interest in the theoretical chemistry community since the late 1970s. Similarly, the Gabor representation has attracted interest in the signal processing community since its invention in 1946, with a peak of interest in the 1980s and 1990s. The development of the theory in these two fields has been nearly independent, with only limited transfer of ideas and methods between these communities. Figure 3a summarizes some of the key milestones in the development of von Neumann/Gabor theory [1, 2, 4, 6–19].

One of the striking parallels in the development of the method in quantum mechanics and signal processing is that the method never became mainstream in either community. A key reason is undoubtedly the problems encountered in converging the method, problems reported independently in both fields. Figure 3b collects some quotations from the literature, both in quantum mechanics and in signal processing, that testify to the problems with convergence of the method [4, 7, 8, 11, 12].

We have recently discovered a simple but surprising way to converge the von Neumann/Gabor method [15–19]. Our insight was to define a modified

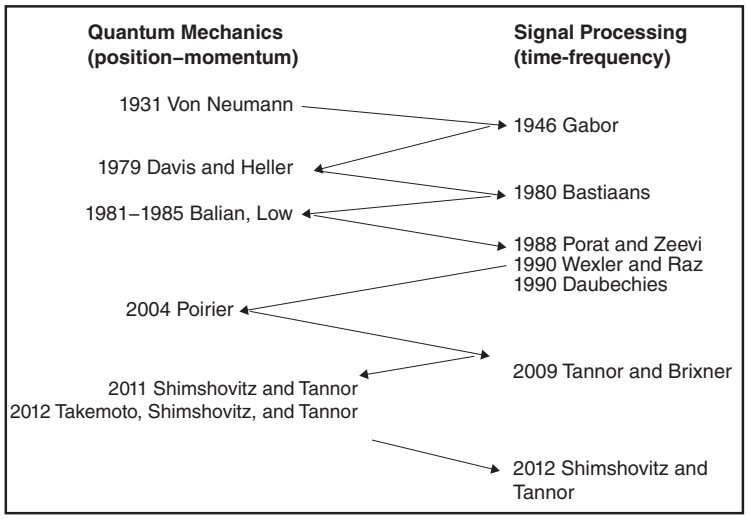

(**a**)

Davis and Heller (1979)

"For γ = l, we have the von Neuman basis, which is very poorly convergent as the grid is extended into phase space."

Balian (1981), Low (1985)

"In order to represent a classical wavepacket, f(x) should go to zero rapidly for large |x|, as should g(p) for large |p|. The requirement of completeness turns out to make this property relatively useless."

Daubechies (1990)

"Gabor's original proposal, with $\omega_0 t_0 = 2\pi$, leads to unstable reconstruction."

Poirier (2004)

"[T]he phase space truncation scheme—tempting though it may be to apply to the von Neumann lattice—is actually quite inefficient in this context."

(**b**)

Figure 3. (**a**) A schematic diagram of the development of the von Neumann/Gabor method in the quantum mechanics and signal processing communities. The development proceeded largely independently. (**b**) Quotes from the quantum mechanics and signal processing literatures indicating that the von Neumann/Gabor basis on a truncated lattice does not converge.

von Neumann/Gabor basis in which the boundary conditions are taken to be periodic and band limited. As we show below, this ensures that the representation has exact informational equivalence with the Fast Fourier Transform method, which has been used so profitably for quantum dynamics calculations. In the language of signal processing, the significance of this result is that the modified Gabor basis

satisfies a Nyquist–Shannon sampling theorem [20–22], meaning that the representation is exact for functions that are band limited and periodic, and converges exponentially fast for functions that decay exponentially in both time and frequency. The net result is that the periodic von Neumann (pvN) or periodic Gabor (pg) basis combines the best of both worlds: Gaussian flexibility with Fourier accuracy.

One more development is crucial to making the method useful. Although the periodic von Neumann representation has complete informational equivalence with the Fourier representation if the full basis is kept, it turns out that discarding even a single pvN function incurs a considerable error—actually a much larger error than incurred in discarding Fourier functions. In other words, Gabor's original proposal for compression turns out not only to fail, but to have exactly the opposite consequences of what he expected. To understand the problem and its solution, note that the von Neumann basis is non-orthogonal. As a result, the basis functions do not satisfy a Kronecker delta relation $\langle g_m | g_n \rangle = \delta_{mn}$, but rather a relation $\langle b_m | g_n \rangle = \delta_{mn}$ where the $\{b_m\}$ are a set of basis functions biorthogonal to the $\{g_n\}$. Although the $\{g_n\}$ are localized the $\{b_m\}$ are not. In the implementation of the vN representation as envisioned by Gabor and all subsequent work, the $\{g_n\}$ are the basis functions and therefore the delocalized $\{b_m\}$ determine the coefficients. Our finding was that by interchanging the role of the basis and its biorthogonal basis we obtain a delocalized basis $\{b_m\}$ but the localized functions $\{g_n\}$ now determine the coefficients, many of which are now nearly vanishing.

The remainder of this review is organized as follows. Section II presents the basic theory. Sections III–V present applications, first to femtosecond pulse shaping, then to quantum mechanics (both time independent and time dependent) and finally to audio and image processing. Section VI is a Conclusion with some discussion of future directions.

II. THEORY

A. von Neumann Basis on the Infinite Lattice

The von Neumann basis set [2] is a subset of the "coherent states" of the form:

$$g_{nl}(x) = \left(\frac{2\alpha}{\pi}\right)^{\frac{1}{4}} \exp\left(-\alpha(x - x_n)^2 + i\frac{p_l}{\hbar}(x - x_n)\right) \tag{1}$$

where n and l are integers. Each basis function is a Gaussian centered at $(x_n, p_l) = (na + x_0, \frac{lh}{a} + p_0)$ in phase space, where x_0 and p_0 are arbitrary shifts. The parameter $\alpha = \frac{\sigma_p}{2\sigma_x}$ controls the FWHM of each Gaussian in x and p space. Taking $\Delta x = a$, $\Delta p = h/a$ as the spacing between neighboring Gaussians in x and p space respectively, we note that $\Delta x \Delta p = h$ so we have exactly one basis function per unit cell in phase space. As shown in [3] this implies completeness in the Hilbert space.

The "complete" vN basis, where n and l run over all integers, spans the infinite Hilbert space. In any numerical calculation, however, n and l take on a finite number of values, producing N Gaussian basis functions $\{g_i(x)\}$, $i = 1 \ldots N$. Since the size of one vN unit cell is h, the area of the truncated vN lattice is given by $S^{\mathrm{vN}} = Nh$.

B. Fourier Method

Before proceeding to describe our modified version of the von Neumann lattice, we need to present some background about the Fourier method.

The pseudospectral Fourier method [23, 24] (also known as the sinc discrete variable representation (DVR) [25]) is a widely used tool in quantum simulations [26–29]. In this method a function $\psi(x)$ that is periodic in L and band limited in $K = \frac{P}{\hbar}$ can be written in the following form: $\psi(x) = \sum_{n=1}^{N} \psi(x_n)\theta_n(x)$, where $x_n = \delta_x(n-1)$, and $\delta_x = \frac{\pi\hbar}{P} = \frac{L}{N}$. The basis functions $\{\theta_n(x)\}$ are given by [30]:

$$\theta_n(x) = \sum_{j=\frac{-N}{2}+1}^{\frac{N}{2}} \frac{1}{\sqrt{LN}} \exp\left(\frac{i2\pi j}{L}(x - x_n)\right), \tag{2}$$

which can be shown to be sinc functions that are periodic on the domain $[0, L]$ [31]. A couple of representative functions from this set are illustrated in Fig. 4.

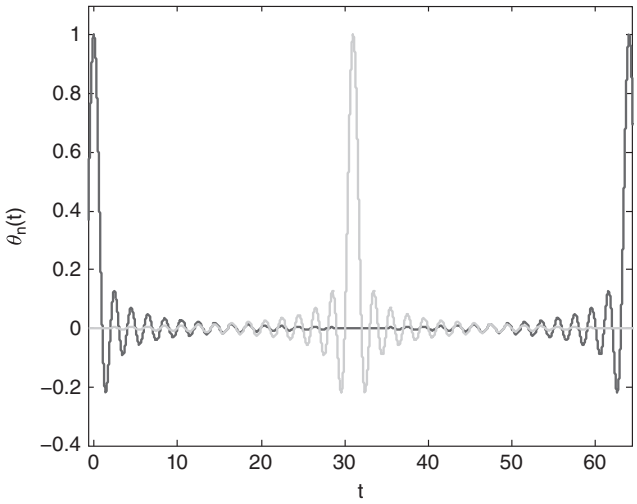

Figure 4. Illustration of the Dirichlet or periodic sinc functions. These functions are the underlying basis of the fast Fourier transform (discrete Fourier transform with periodic boundary conditions). They go to 1 at one of the Fourier grid points and to 0 at all the other Fourier grid points. The various members of the basis are orthonormal. For a color version of this figure, see the color plate section.

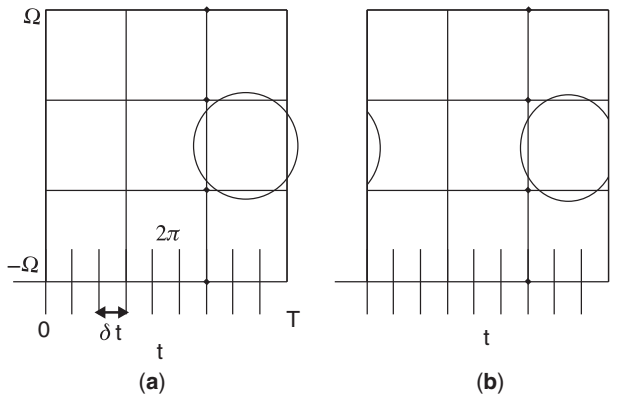

Figure 5. (**a**) $N = 9$ coordinate grid points and $N = 9$ Gabor unit cells cover the same area in phase space, $S = 2\pi N$. Superimposed is a typical Gabor function. Note that its boundary conditions are not appropriate for the rectangular area. (**b**) The periodic Gabor (pg) basis is a complete set for the truncated space. The pg basis functions are, loosely speaking, periodic and band-limited Gaussians whose centers are located at the center of each unit cell.

By Nyquist's theorem, if the spacing between points in the Fourier method is δx, the frequency range that can be spanned is $2P = 2\frac{\pi\hbar}{\delta_x}$. Thus, the set $\{\theta_i(x)\}$ $i = 1, \ldots, N$ spans a rectangular shape in phase space with area $S^{\mathrm{FGH}} = 2LP = 2L\frac{\pi\hbar}{\delta_x} = Nh$ [23]. Thus N unit cells in the vN lattice and N grid points in the Fourier method cover the same rectangle with an area in phase space of (Fig. 5a):

$$S^{\mathrm{vN}} = S^{\mathrm{FGH}} = Nh. \tag{3}$$

This suggests that N vN basis functions confined to this area will be equivalent to the Fourier basis set. Unfortunately, the attempt to use N Gaussians as a basis set for this phase space area leads to extremely large numerical errors. One may think of this as a result of Gaussians on the edges of Fig. 5a protruding from the truncated space; as a consequence, there are also gaps in the coverage of the Hilbert space of the interior region.

C. The Periodic von Neumann Basis (pvN)

The problem with convergence of the truncated lattice of Gaussians can be overcome by combining the Gaussian and the Fourier basis functions, generating a "Gaussian-like" basis set that completely spans the truncated space. Specifically,

the $\{g_m(x)\}$ functions enter as the coefficients of the Dirichlet functions $\{\theta_i(x)\}$ to construct a new basis set, $\{\tilde{g}_m(x)\}$:

$$\tilde{g}_m(x) = \sum_{n=1}^{N} \theta_n(x) g_m(x_n) \tag{4}$$

for $m = 1, \ldots, N$. The new basis set is in some sense, the Gaussian functions with periodic boundary conditions and band limited, henceforth the periodic von Neumann or pvN basis (Fig. 5b). We can write Eq. (4) in matrix notation as: $\tilde{\mathbf{G}} = \Theta\mathbf{G}$, where $G_{ij} = g_j(x_i)$. By taking the width parameter $\alpha = \frac{\Delta p}{2\hbar\Delta x}$ we guarantee that the pvN functions have no linear dependence and that the matrix $\mathbf{G}$ is invertible, that is $\tilde{\mathbf{G}}\mathbf{G}^{-1} = \Theta$. The invertibility of $\mathbf{G}$ implies that the $\{\tilde{g}_m(x)\}$ and the $\{\theta_i(x)\}$ span the same Hilbert space and therefore are informationally equivalent representations.

Inspection of Fig. 5b explains why the subtitle of this review is "thinking inside the box."

D. Biorthogonal von Neumann Basis Set (bvN)

Although the pvN and the Fourier methods span the same rectangle in phase space, in the Fourier basis one is constrained to a rectangular area in phase space whereas in the pvN method one has the freedom to place basis functions only where needed in phase space. If the classical phase space up to energy E occupies only a small fraction of the circumscribed rectangular area, the pvN basis can lead to significant savings. This is particularly important for multidimensional problems, where the savings in the pvN actually grows faster than exponentially with dimension, as discussed in Section II E. below. However, there is an important subtlety in discarding basis functions that arises because the basis in non-orthogonal. We therefore provide a brief review of some properties of non-orthogonal bases.

For an orthonormal basis, we have the relation:

$$\langle \phi_m | \phi_n \rangle = \delta_{mn}. \tag{5}$$

For a non-orthogonal basis this relation does not in general hold and one writes:

$$\langle g_m | g_n \rangle = S_{mn}, \tag{6}$$

where $\mathbf{S}$ is the overlap matrix. Alternatively, one can write:

$$\langle b_m | g_n \rangle = \langle g_m | b_n \rangle = \delta_{mn} \tag{7}$$

where the set $\{b_m\}$ is called the basis "biorthogonal" to the set $\{g_n\}$. The usual completeness relation for orthogonal bases:

$$\sum_{n=1}^{\infty} |\phi_n\rangle\langle\phi_n| = \mathbf{1} \tag{8}$$

is replaced by the relations:

$$\sum_{n=1}^{\infty} |g_n\rangle\langle b_n| = \sum_{n=1}^{\infty} |b_n\rangle\langle g_n| = \mathbf{1}. \tag{9}$$

To obtain an explicit relation for the $\{b_n\}$ we note the following alternative expression for the completeness relation for a non-orthogonal basis [32]:

$$\sum_{n=1}^{\infty}\sum_{m=1}^{\infty} |g_m\rangle(S^{-1})_{mn}\langle g_n| = \mathbf{1}. \tag{10}$$

Comparing Eq. (10) with Eq. (9) we see that

$$|b_n\rangle = \sum_{m=1}^{\infty} |g_m\rangle(S^{-1})_{mn}, \tag{11}$$

or on the truncated space

$$|\tilde{b}_n\rangle = \sum_{m=1}^{N} |\tilde{g}_m\rangle(S^{-1})_{mn}. \tag{12}$$

Figure 6 shows a plot of the $\mathbf{S}$ and the $\mathbf{S^{-1}}$ matrices on a logarithmic scale. As seen clearly in the figure, although the $\mathbf{S}$ matrix is tightly banded, the $\mathbf{S^{-1}}$ decays slowly away from the diagonal. As a consequence, although the $\{g_i\}$ basis is localized, the $\{b_i\}$ basis is delocalized. Figure 7 shows a typical b_n basis function, which is seen to be not only delocalized but to be quite irregularly shaped with discontinuous derivatives.

E. Periodic von Neumann Basis with Biorthogonal Exchange (pvb)

We now return to the issue of discarding unnecessary basis functions. If $|\psi\rangle$ occupies only a fraction of the rectangle spanned by the Fourier basis, we may expect that many of the pvN basis functions will fulfill the relation: $\langle\tilde{g}_j|\psi\rangle = 0$, $j = 1, \ldots, M$. However, due to the non-orthogonality of the basis we cannot simply

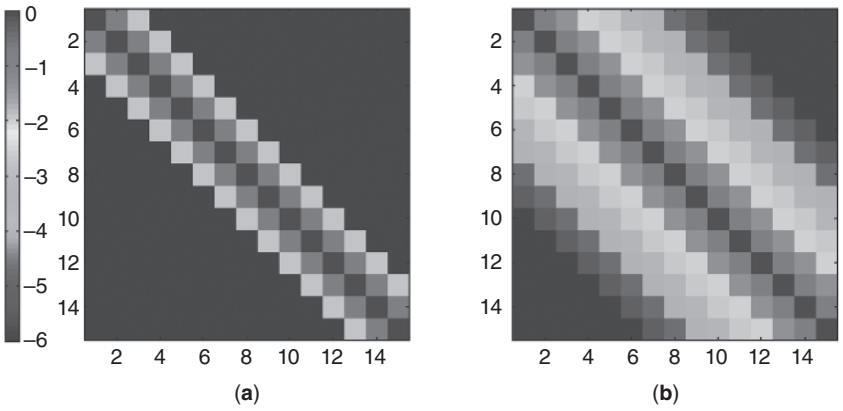

Figure 6. Magnitude of **S** (**a**) and $\mathbf{S^{-1}}$ (**b**) matrices on a logarithmic scale. For a color version of this figure, see the color plate section.

eliminate the states $\tilde{g}_j$, since the *coefficients* of $\tilde{g}_j$ are not simply given by $\langle \tilde{g}_j|\psi\rangle = 0$. To see this, consider the representation of the state $|\psi\rangle$ in the pvN basis set:

$$|\psi\rangle = \sum_{m=1}^{N} |\tilde{g}_m\rangle a_m = \sum_{n=1}^{N}\sum_{m=1}^{N} |\tilde{g}_m\rangle (S^{-1})_{mn}\langle \tilde{g}_n|\psi\rangle, \tag{13}$$

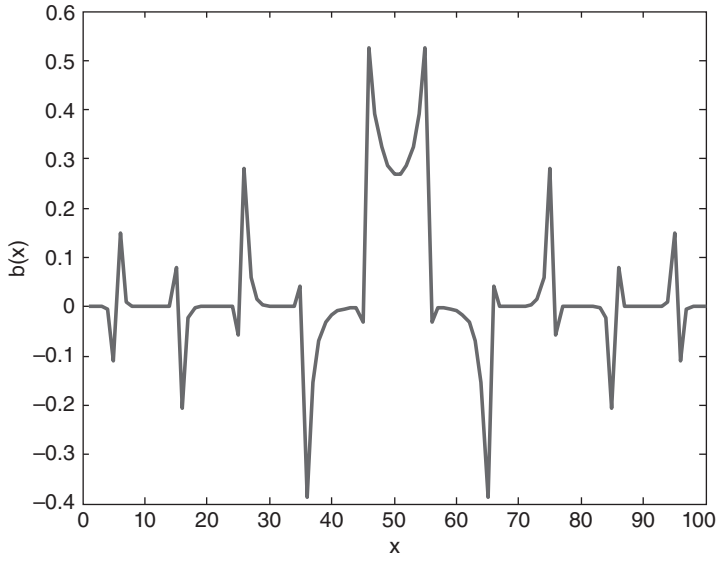

Figure 7. A typical biorthogonal basis function.

where in the second equality we have used the completeness relationship for non-orthogonal bases, Eq. (10), applied to the truncated space. Comparing the two expressions in Eq. (13) we find that

$$a_m = \sum_{n=1}^{N} (S^{-1})_{mn} \langle \tilde{g}_n | \psi \rangle. \tag{14}$$

The expression for the coefficients a_m is seen to contain $\mathbf{S^{-1}}$. Since as discussed above $\mathbf{S^{-1}}$ is delocalized, a_m can be quite significant, even if g_m is remote from ψ because a_m can draw amplitude from non-remote $\langle \tilde{g}_n | \psi \rangle$. Nevertheless, we can still take advantage of the many near-vanishing $\langle \tilde{g}_n | \psi \rangle$ to obtain a compact representation of the function $|\psi\rangle$. The key is to exchange the role of the $\{g_n\}$ and $\{b_m\}$ basis sets. Substituting Eq. (12) into Eq. (13), $|\psi\rangle$ can be written as

$$|\psi\rangle = \sum_{n=1}^{N} |\tilde{b}_n\rangle c_n = \sum_{n=1}^{N} |\tilde{b}_n\rangle \langle \tilde{g}_n | \psi \rangle. \tag{15}$$

By assumption, M of the coefficients are zero, hence only $N' = N - M$ basis functions are necessary in order to represent $|\psi\rangle$ in this basis. Note that the new basis functions, the $\{b_n\}$, are not only delocalized but have discontinuous derivatives (see Fig. 7); paradoxically, this is the farthest thing from the localized basis envisioned by Gabor and by his counterparts in the quantum community! However, this highly irregular basis is exactly what is needed to ensure that the localized functions $\{g_n\}$ determine the coefficients, and hence that the representation is as sparse as possible.

The equations take a particularly compact form in matrix notation: Eq. (12) becomes $\mathbf{B} = \mathbf{G}\mathbf{S^{-1}} = (\mathbf{G}^\dagger)^{-1}$ or $\mathbf{G}^\dagger\mathbf{B} = \mathbf{1}$ at the Fourier grid points.

The biorthogonal basis is well known in the signal processing literature [6, 9, 10, 33–35], but the crucial idea of exchanging the roles of the pvN and the bvN seems to have been overlooked. We attribute this to the fact that Eq. (10) involving $\mathbf{S^{-1}}$ does not appear in that literature. It is this expression, together with the non-sparseness of the $\mathbf{S^{-1}}$ matrix that provides the motivation for the exchange of roles. To distinguish our method from previous work we call our method the "periodic von Neumann with biorthogonal exchange" method or pvb. When applying the method to signal processing we refer to it as the "periodic Gabor with biorthogonal exchange" method or pgb.

III. APPLICATION TO ULTRAFAST PULSES

As a first illustration of the use of the periodic Gabor basis we consider the representation of shaped femtosecond laser pulses that emerge in the field of quantum

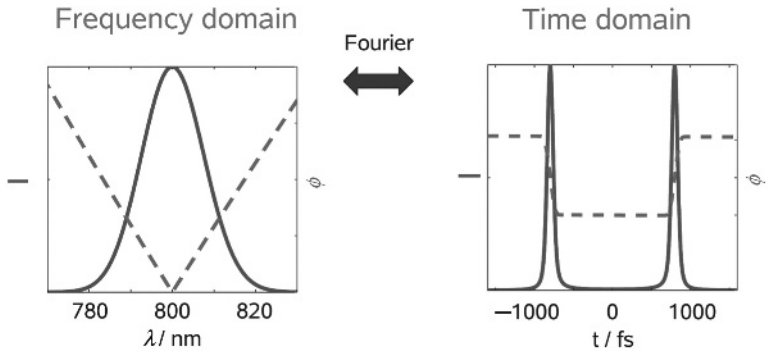

Figure 8. Example of a non-intuitive Fourier transform pair. The solid line shows the amplitude and the dashed line the phase. The "V" phase profile in frequency leads to a double-pulse structure in time.

control [36–41]. These pulses are complex, and in general are shaped in both amplitude and phase. We start with this example for three reasons. First, chronologically this was our first application of the von Neumann lattice [14,15]. Second, it provides a nice comparison of the visual form of the discrete Gabor representation with the Wigner and Husimi representations. Third, it shows the importance of the periodic boundary conditions in the Gabor representation without the additional complications of quantum mechanical operators. In Section IV, when we turn to the quantum mechanical applications, all the considerations introduced in this section will still apply, with additional methods required to represent operators in the pvb basis.

Figure 8 shows a shaped laser pulse in both the frequency and time representations. In frequency, it consists of a Gaussian amplitude multiplied by a "V" phase profile. In the time domain, related by a Fourier transform, the "V" phase profile leads to a double-pulse structure. Although both the frequency and time representations contain the same information, it is difficult to appreciate all the properties of the signal from one representation alone.

Figure 9a shows the same signal in the Wigner representation [42]. The marginals of the Wigner representation give the absolute value squared in the frequency and time representations, respectively. However, in the Wigner representation one can visualize simultaneously both the single-lobed structure of the frequency profile and the double-lobed structure of the time profile. Note that the Wigner representation shows oscillations between the two portions of the pulse in time. These oscillations can take on negative values, making it impossible to interpret the Wigner representation strictly as a probability distribution. Figure 9b shows the Husimi representation of the same signal. The Husimi representation is defined as the absolute value squared of the overlaps of the signal with a continuous-parameter set of time–frequency Gaussians [43], and therefore unlike

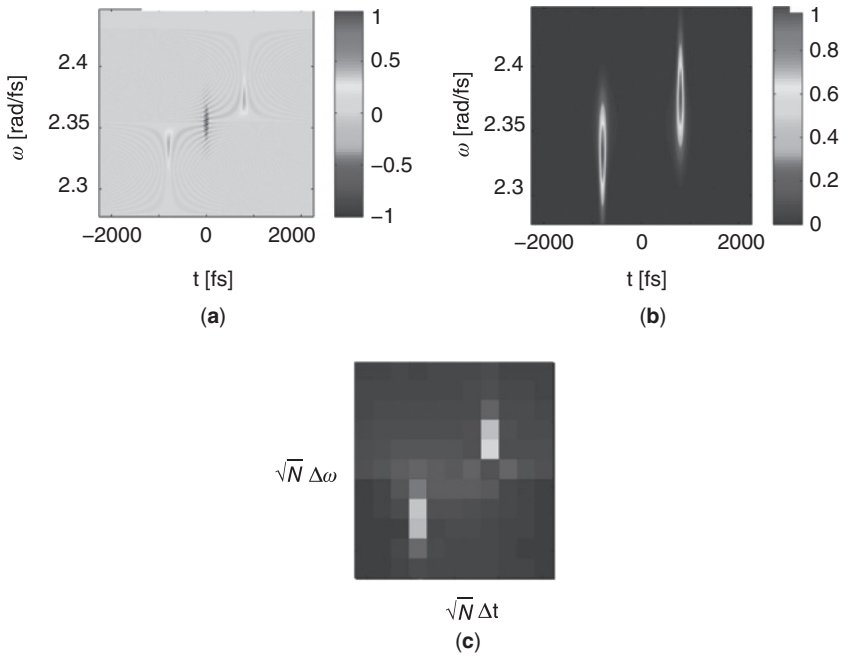

Figure 9. The Wigner representation (**a**), the Husimi representation (**b**), and the von Neumann representation (**c**) of the pulse in Fig. 8. All three representations allow the visualization of the pulse in time and frequency simultaneously. For a color version of this figure, see the color plate section.

the Wigner representation is everywhere positive semidefinite. Formally, one can show that the Husimi representation is a Gaussian smoothing of the Wigner representation, and in fact one can see that the oscillations in the Wigner representation are washed out in the Husimi representation.

Figure 9c shows the signal of Fig. 8 in the von Neumann/Gabor representation. Since the basis set is discrete so is the representation. The major features of the signal in both frequency and time are clearly observed. The discreteness of the representation, which at first sight may appear somewhat jarring, is actually its strength, providing exactly the same number of parameters as the discrete Fourier representation.

As a first test of the von Neumann representation, in Fig. 10 we consider whether the transformation of a signal to the von Neumann representation is invertible. The red curve in Fig. 10c portrays the amplitude profile of a frequency signal defined at a finite, discrete number of points. Such a discrete representation occurs naturally when considering shaped ultrafast pulses, since the masks used for pulse shaping consist of a finite, discrete number of pixels. Figure 10a–b show the amplitude and phase respectively of the von Neumann representation. The back-transformed signal is shown as the blue curve in Fig. 10c, and differs significantly from the

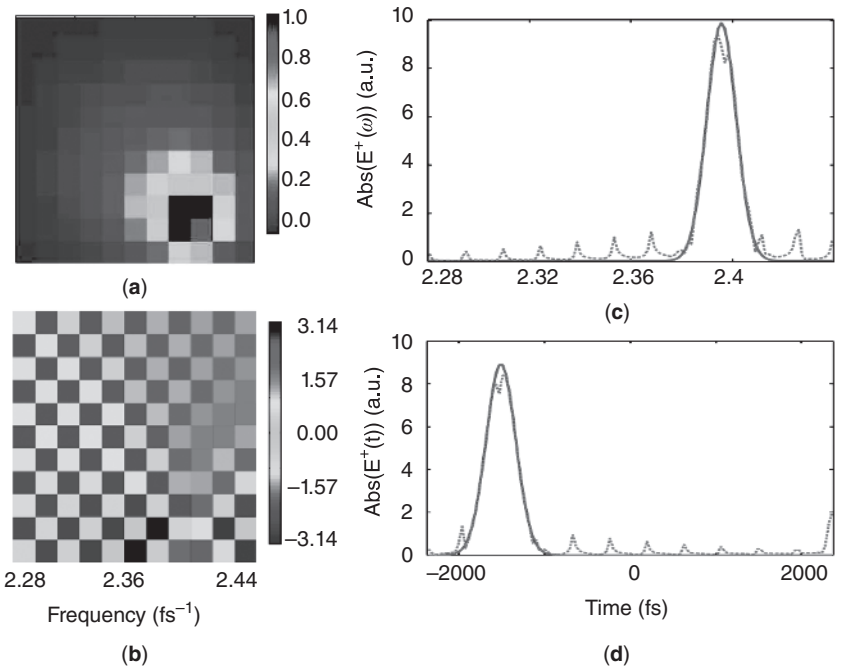

Figure 10. Transformation of a Gaussian pulse from frequency to the von Neumann representation and back without periodic boundary conditions. The error in the back-transformed signal is quite significant (blue vs. red curve in (**c**)). Panel (**a**) shows the amplitude of the von Neumann representation and panel (**b**) the phase. Adapted from Ref. [15]. For a color version of this figure, see the color plate section.

original signal. However, when the conventional von Neumann basis is replaced by the pvN basis, the representation in Fig. 11a–b is obtained. The periodic boundary conditions are clearly visible in the figure, with the effect that the ringing in the interior region that is present Fig. 10a is eliminated. When Fig. 11a is back-transformed to frequency, the signal is indistinguishable from the original (red curve in Fig. 11c), and in fact the two signals are identical to the precision of the computer. This shows the dramatic effect of the periodic boundary conditions on the von Neumann representation.

IV. APPLICATIONS TO QUANTUM MECHANICS

We now turn to the main topic of this review, the application of the pvb method to quantum mechanics. In this section we discuss the application to the TISE and in the next section we will discuss the application to the time-dependent Schrödinger equation.

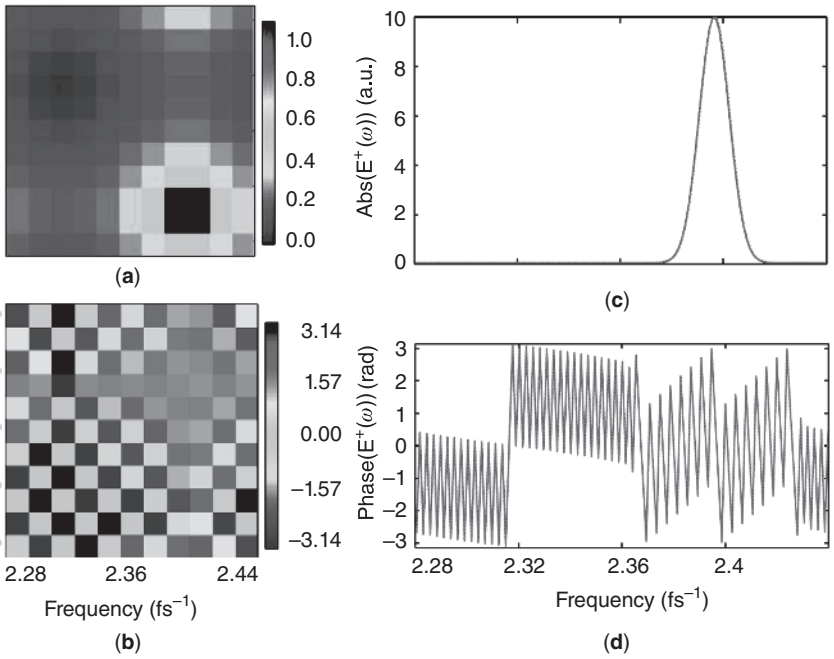

Figure 11. Transformation of a Gaussian pulse from frequency to the von Neumann representation and back with periodic boundary conditions. The back-transformed signal agrees with the original signal to the accuracy of the computer (blue vs. red curve in (**c**)). Panel (**a**) shows the amplitude of the von Neumann representation and panel (**b**) the phase. Adapted from Ref. [15]. For a color version of this figure, see the color plate section.

A. Time-independent Schrödinger Equation (TISE)

1. Formalism

Consider the TISE $H\Psi = E\Psi$. H is the Hamiltonian operator consisting of a kinetic energy and a potential energy operator: $H = T + V = -\frac{\hbar^2\partial^2}{2m\partial x^2} + V(x)$ where for simplicity we use a 1D notation and express the operator in the coordinate representation. In a non-orthogonal basis this equation takes the form:

$$\mathbf{HU} = \mathbf{SUE} \tag{16}$$

where **H** is the Hamiltonian matrix whose elements H_{ij} are given by

$$H_{ij} = \langle g_i|H|g_j\rangle = \int_{-\infty}^{\infty} g_i^*(x)\left[-\frac{d^2}{dx^2} + V(x)\right] g_j(x)dx \tag{17}$$

and **S** is the overlap matrix defined in Eq. (16)

$$S_{ij} = \langle g_i | g_j \rangle = \int_{-\infty}^{\infty} g_i^*(x) g_j(x) dx. \tag{18}$$

In the pvN basis, the basis functions $\{g_i\}$ take the form $\{\tilde{g}_i\}$ given by Eq. (4), so Eq. (18) takes the form [16]:

$$\begin{aligned} S_{ij} = \langle \tilde{g}_i | \tilde{g}_j \rangle &= \int_0^L \tilde{g}_i^*(x) \tilde{g}_j(x) dx \\ &= \sum_{n=1}^{N} \sum_{m=1}^{N} g_i^*(x_n) g_j(x_m) \int_0^L \theta_n^*(x) \theta_m(x) dx \\ &= \sum_{n=1}^{N} g_i^*(x_n) g_j(x_n). \end{aligned} \tag{19}$$

Note that the tildes completely disappear from the expression for S_{ij} and one is left only with the sampling of the original Gaussians at the Fourier points. In matrix notation, Eq. (19) takes the form

$$\mathbf{S} = \mathbf{G}^\dagger \mathbf{G}. \tag{20}$$

In the pvN basis the Hamiltonian matrix takes the form [16]:

$$\begin{aligned} H_{ij}^{\text{pvN}} &= \langle \tilde{g}_i | H | \tilde{g}_j \rangle \\ &= \sum_{m=1}^{N} \sum_{n=1}^{N} g_i^*(x_m) \langle \theta_m | H | \theta_n \rangle g_j(x_n) \\ &= \sum_{m=1}^{N} \sum_{n=1}^{N} g_i^*(x_m) H_{mn}^{\text{FGH}} g_j(x_n) \end{aligned} \tag{21}$$

and similarly

$$H_{ij}^{\text{bvN}} = \sum_{m=1}^{N} \sum_{n=1}^{N} b_i^*(x_m) H_{mn}^{\text{FGH}} b_j(x_n). \tag{22}$$

Again, note that the tildes completely disappear in both the pvN and bvN representations, as a result of the orthonormality of the θ_m. We have made use of the fact that $\langle \theta_m | H | \theta_n \rangle$ is precisely what is meant by the Fourier grid Hamiltonian

[24]: $H^{\mathrm{FGH}} = V^{\mathrm{FGH}} + T^{\mathrm{FGH}}$, where the potential and the kinetic energy matrices are given by: $V_{ij}^{\mathrm{FGH}} \approx V(x_i)\delta_{ij}$ and [44]

$$T_{ij}^{\mathrm{FGH}} = \frac{\hbar^2}{2M} \begin{cases} \dfrac{K^2}{3}\left(1 + \dfrac{2}{N^2}\right), & \text{if} \quad i = j \\ \dfrac{2K^2}{N^2} \dfrac{(-1)^{j-i}}{\sin^2\left(\pi \frac{\mathrm{j-i}}{\mathrm{N}}\right)}, & \text{if} \quad i \neq j. \end{cases} \tag{23}$$

2. 1D Applications

To illustrate the importance of the periodic boundary conditions, we start with a simple example of the 1D harmonic oscillator. Figure 12a shows the error in the seventh eigenvalue of the harmonic oscillator as a function of the basis set size N for a rectangular phase space grid. The results using the vN basis without periodic boundary conditions converge extremely slowly. In contrast, the results using the Fourier grid, the pvN and the pvb methods all converge exponentially, and in fact give identical results as long as a rectangular phase space lattice is used. The poor convergence of the conventional vN method can be understood by considering Fig. 12b, which compares the kinetic energy spectrum obtained using the FGH/pvN/bvN representations with that obtained using the conventional vN representation. The eigenvalues of the kinetic energy matrix using

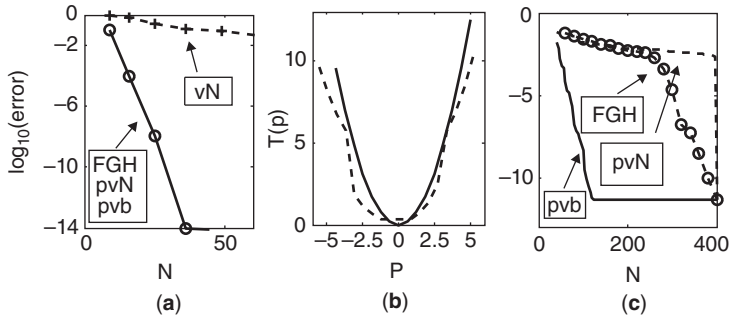

Figure 12. (**a**) Error in the seventh eigenvalue of the harmonic oscillator for a rectangular phase space grid as a function of the basis set size N. The pvN, pvb, and Fourier grid methods all give identical results (solid), 14 orders of magnitude more accurate than the usual vN basis (dashed). (**b**) Kinetic energy spectrum using the vN basis(dashed) and using the FGH, pvN, and bvN basis (solid). (**c**). Error in the 24th eigenvalue of the Morse potential as one discards basis functions from a rectangular phase space lattice. The pvb (solid), pvN (dashed), and Fourier grid (dotted) behave completely differently. Removing even one basis function from the pvN introduces significant error, while more than two-thirds of the pvb basis functions can be removed without introducing any significant error. Adapted from Ref. [16].

the FGH/pvN/bvN methods trace out a truncated parabola. Although the kinetic energy spectrum is truncated at a value of $T_{\max}$ determined by the spacing δx, the spectrum is exact within the domain determined by the truncation. In contrast, the eigenvalues obtained with the vN method describe a corrugated parabola. This error in the kinetic energy (and a similar error in the potential energy) leads to an error in the energy eigenvalues.

Having shown that the FGH/pvN/bvN methods all give identical results for a rectangular phase space, we now ask what happens when one begins to remove basis functions. Figure 12c shows the error in the 24th eigenvalue of a 1D Morse potential as one discards basis functions from a rectangular phase space lattice. The pvN (dashed), pvb (solid), and Fourier grid (dotted) behave completely differently: removing even one basis function from the pvN introduces a significant error, an error much larger than removing basis functions from the FGH method. However, by exchanging the roles of the basis and its biorthogonal basis, more than two-thirds of the pvb basis functions can be removed without introducing any significant error.

3. Multidimensional Applications

Formally, the extension of the pvN and pvb methods to multidimensions is straightforward if the full multidimensional rectangular basis is kept. The overlap matrix and the kinetic energy matrix become tensor products of 1D overlap and kinetic energy matrices, respectively, and the multidimensional V matrix is diagonal. However, the key to large savings in multidimensions is to avoid a tensor product representation. In fact, one wants to avoid constructing tensor product matrices even as intermediates, since in multidimensions these can easily exceed the size of even the largest computer memories.

Thus, one of the key practical issues is choosing an optimal non-direct Hilbert space, that is, knowing in advance which basis functions in the tensor product Hilbert space can be discarded. If one has already solved the TISE and has the exact eigenfunctions the answer is straightforward: the overlaps of the phase space Gaussian with the exact eigenfunctions can be used to determine which biorthogonal functions should be eliminated from the basis. But this presumes that the solutions of the TISE are already known, knowledge that is generally lacking. We have therefore tested a number of alternative criteria. A simple and intuitive approach is to choose a cutoff based on the energy of the center of the Gaussian, but this was found not to give very accurate results. A second approach is to calculate the distance of the center (or perhaps the tail) of the Gaussian from the classical energy contour, and this indeed gives higher accuracy. A third approach, which looks promising in preliminary tests, is to calculate the eigenfunctions using a small basis, and use the crude eigenfunctions as a guide for adding additional basis functions. This approach can be applied iteratively, adding additional layers of basis functions until a desired level of convergence is achieved.

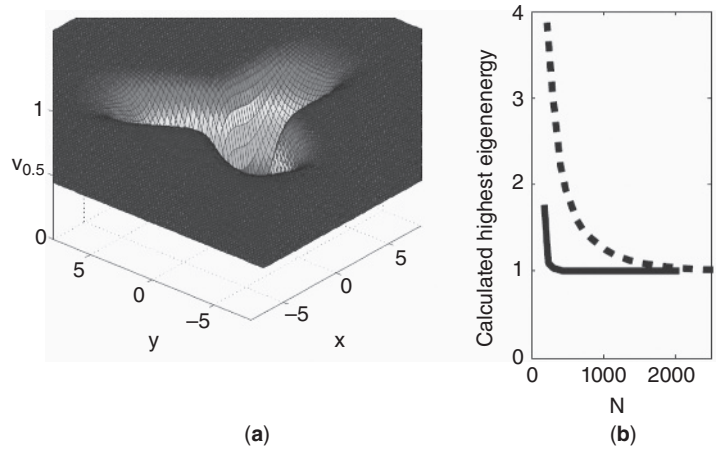

Figure 13. (**a**) The triangle potential. (**b**) Comparison of the error in the highest eigenvalue of the Fourier (dashed) and pvb (solid) methods as a function of basis set size. Adapted from Ref. [16]. For a color version of this figure, see the color plate section.

As mentioned above, one wants to avoid constructing tensor product matrices even as intermediates. The tensor product matrices can be avoided by building the compact pvb matrices directly, element by element. Somewhat surprisingly, the computational bottleneck in multidimensions turns out to be constructing the diagonal **V** matrix. A promising approach seems to be to write the multidimensional potential as a sum of factorized 1D potentials. Then the construction of the **V** matrix proceeds essentially in the same way as the construction of the **T** matrix.

As an example of the application of the pvb method to a multidimensional system, consider the 2D "triangle" potential shown in Fig. 13a. This potential has threefold rotational symmetry which is characteristic of the potential in the 2D degenerate subspace of a molecule with a threefold axis of symmetry. The potential has the same symmetry as the Henon–Heiles potential, but is a bona fide bound potential as opposed to the Henon–Heiles which is metastable. Moreover, we designed this potential to have elongated troughs, and therefore it is much less harmonic than the Henon–Heiles. We have chosen the parameters so that the potential dissociates at $E = 1$ and has 10,000 bound states.

Figure 13b compares the error in the highest eigenvalue of the triangle potential as a function of basis set size for the pvb and FGH methods. The pvb method is seen to provide the same accuracy as the FGH method, using only about one-tenth of the number of basis functions.

Multidimensional applications to LiCN, HCN, and HCCH are in progress but have not been published yet [45]. Preliminary results indicate that the

multidimensional pvb is always more efficient that the multidimensional FGH (the comparison assumes that the FGH basis is pruned in coordinate space where the value of the potential is high [25]). However, the savings of the pvb for these systems is found to be somewhat lower than for the triangle potential, since these molecular potentials are closer to harmonic, where the pvb savings is smaller. The pvb method is also found to be less efficient than the successive diagonalization/truncation scheme [46], where the latter can be performed. The real advantage of the pvb method is that it does not require any zeroth order separation of the Hamiltonian or assumption about adiabaticity of some modes: it performs the pruning of basis functions in all degrees of freedom at once, in an automated way without the need to set up a hierarchy of modes. Because it adapts the basis to the classical phase space boundary, not just the coordinate space boundary, it is expected to provide roughly speaking the square of the savings of an FGH basis with coordinate space pruning (2 degrees of freedom per coordinate instead of just 1).

4. Scaling of the Method with h and with Dimensionality

The ability to localize a pvb function at a specific point in phase space results in the remarkable concept that in the classical limit one requires only one basis function per eigenstate. In other words, to calculate N eigenenergies we should need only N basis functions. This limit can be understood as follows. Semiclassically, a classical phase space volume V supports $N = V/h$ eigenstates, that is, every eigenstate spans a phase space volume of h (or in multidimensions, h^D). However, every vN basis function spans a phase space volume of h, hence N vN basis functions span a phase space volume V. In the limit that the size of the Planck cell h is much smaller than the phase space volume V, so that the edge effects from the pruned lattice can be neglected, the vN basis exactly covers the classical phase space. But this is the limit $V \gg h$, which is precisely what is meant by the classical limit. This remarkable property is unique for methods based on phase space localization [13].

Figure 14a shows the classical phase space for the Morse oscillator up to a particular value of E, tiled using phase space squares. The squares that cover the classical phase space are a qualitative guide to the placement of Gaussian basis functions. It is seen that in the case of the 1D Morse oscillator, the pvb basis needed will be only about half the size of the full phase space lattice and therefore of the FGH basis. As shown in Fig. 14b, as $h \to 0$ the pvb method approaches efficiency 1 while the efficiency of the FGH method (the inverse of the number of converged eigenvalues per basis functions) is the ratio of the classical phase space to the circumscribed rectangle.

In the classical limit, one can study the efficiency as a function of dimensionality. Consider the harmonic oscillator system. In 1D, the ratio of the classical phase space to the FGH method is the ratio of the area of a circle inscribed in a square,

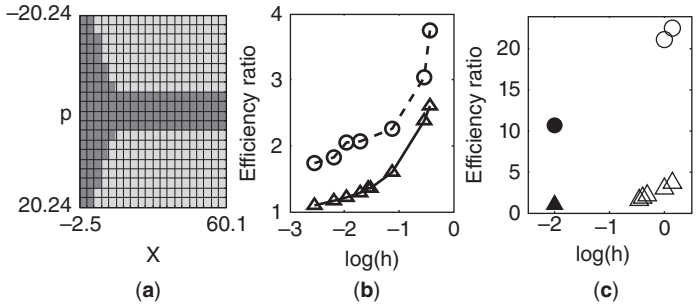

Figure 14. (**a**) Phase space area spanned in the bvN method (magenta) and in the pvN (or FGH) method (full rectangle) for a 1D Morse oscillator Morse. (**b**) Efficiency ratio (defined as number of basis functions per converged eigenstates) of the bvN (solid) and FGH (dashed) methods for the 1D Morse oscillator as a function of h. (**c**) Efficiency ratio of the bvN (triangles) and FGH (circles) methods for the 2D triangle potential of Fig. 13 as a function of h. The solid triangle and circle are the efficiencies in the classical limit. Adapted from Ref. [16]. For a color version of this figure, see the color plate section.

$\eta = \frac{\pi}{4}$. In multidimensions this generalizes to the volume of a D-dimensional sphere inscribed in a D-dimensional cube which takes the value:

$$Ratio = \frac{\eta^D}{D!}. \tag{24}$$

The $D!$ scaling formally defeats the exponential wall with dimensionality. This is discussed in more detail in [31], where an intuitive explanation of the origin of the $D!$ factor is provided and shown to be generally an underestimate—potentially by a very large factor—of the actual factor that arises from the multidimensionality of the phase space.

5. Wavelet Generalization

Returning to Eq. (4), we note that it permits a wide variety of generalizations. First, the θ functions are not required to be Dirichlet functions—any set of localized, orthonormal functions can be used, for example, DVR functions. We have tested Eq. (4) with Gauss–Legendre θ functions in the angle and Dirichlet functions in the radial coordinate(s) to calculate the vibrational levels of LiCN in 2D and of HCN in 3D. As mentioned above, these results are as yet unpublished but show that the pvb representation can be significantly more efficient than the tensor product FGH and DVR representations, even when the latter are implemented with coordinate space pruning.

Another generalization of Eq. (4) is that functions $\{g_i\}$ on the right-hand side of the equation could be any phase space localized functions, not necessarily Gaussians. Alternatively, they could be Gaussians but with unequal spacing and

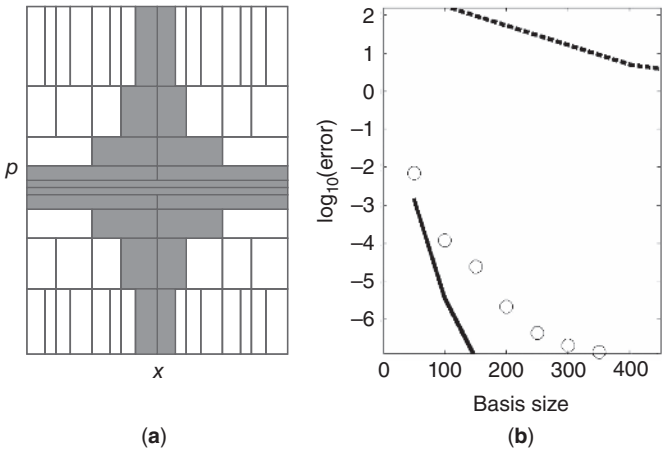

Figure 15. (**a**) The periodic von Neumann method does not require identical, evenly spaced Gaussians. One may tile the phase space any way one likes as long as the rectangular tiles have area h. Then a basis of Gaussians whose centers and aspect ratios are matched to the rectangles will be a complete and stable basis. This flexibility in the positions and widths of the Gaussians can improve the efficiency of the pvN method significantly, particularly for problems that have multiple length scales. (**b**) The error in E_3 for the Coulomb potential as a function of basis set size. FGH (dashed), pvb (circles), and wpvb (solid). Adapted from Ref. [17].

widths. Mathematically, the only requirement to obtain equivalence with the FGH method is that the N functions be linearly independent; however in practice, we have found that for numerical stability the functions should correspond to a complete tiling of the FGH phase space using N tiles, each of area h. One way to produce such a tiling is to use rectangles that satisfy a scaling relationship as shown in Fig. 15a. Then one Gaussian is placed in each phase space rectangle with an aspect ratio matched to the aspect ratio of the rectangle [17]:

$$g_{nl}(x) = \left(\frac{2\alpha_l}{\pi}\right)^{\frac{1}{4}} \exp\left(-\alpha_l(x - x_{nl})^2 + \frac{ip_l}{\hbar}(x - x_{nl})\right), \tag{25}$$

where $a_l = ab^{|l|-1}$, $x_{nl} = (n - \frac{1}{2})a_l + x_1$, $p_l = \frac{2\pi\hbar}{a_l}(\frac{b^l - 1}{b-1} - \frac{1}{2})$ $(l > 0)$, $p_l = -p_{-l}$ $(l < 0)$ and x_1 is the first point of the Fourier grid. The indices n, l take the values $n = 1, \ldots, N_x^l$, $l = \pm 1, \ldots, \pm N_p$ where N_x^l is the number of Gaussians at each p level, given by the ratio $N_x^l = \frac{L}{a_l}$ and N_p is the number of scales. The total number of Gaussians is $\sum_l N_x^l = N$. We call this approach "wavelet pvb" or wpvb.

To see where such a scaling of the basis could be useful, consider the phase space of the 1D Coulomb potential, shown in Fig. 2b. The phase space has long tails at large $|x|$ and extends to high $|p|$ at small $|x|$. Tiling the classical phase

space as in Fig. 15a will require many fewer tiles than using equidistant, identical Gaussians. Figure 15b compares the error as a function of basis set size for the FGH, pvb, and wpvb methods. The wpvb method is seen to significantly reduce the error relative to the pvb method. Johnson and Kinsey have explored the use of Daubechies wavelets [11] to solve the TISE [47]. Preliminary results show that the wpvb method is significantly easier to use and slightly more accurate, but further testing would be desirable.

It is interesting to compare the pvN and wpvN methods with two other methods: the distributed Gaussian method [48–50] and the mapped Fourier method [51]. The distributed Gaussian method tailors the width of the Gaussians to the local potential and therefore would seem to have something in common with the wpvN method. However, as opposed to the wpvN there is no systematic procedure for distributing the Gaussians in multidimensions; moreover, because there is no periodicity in the boundary conditions the method necessary requires overcompleteness in order to converge. The mapped Fourier method seeks a mapping of the coordinates so that the classical phase space will be as close as possible to rectangular. Then the corresponding mapping is applied to the quantum Hamiltonian. Again, there is no systematic procedure known for performing the mapping in multidimensions, and in practice the method has been found to have limited accuracy for some prototypical systems, such as the Coulomb potential.

B. Time-dependent Schrödinger Equation (TDSE)

The pvb method can also be applied to solving the TDSE, in the presence of time-dependent fields. The concept of the classical phase space as a guide for where to place basis functions still applies, but now the classical phase space and the corresponding quantum mechanical basis depend on time. Two key issues arise. First, should the basis functions be allowed to evolve in time or only the coefficients? A great deal of effort has gone into developing methods to solve the TDSE in a basis of moving Gaussians. In some of these methods the Gaussians evolve according to classical mechanics [52, 53] and in others there are quantum corrections to the evolution or the evolution is determined by a set of coupled variational equations [54–58]. The motivation for a classically evolving basis is that to the extent that classical–quantum correspondence applies to the Gaussians either individually or to their collective distribution, the moving basis should cover the requisite quantum phase space as a function of time.

We have decided to take a different approach, in which the Gaussian basis is fixed and only the coefficients change in time [18]. Our motivation is several fold: 1. As we have seen in the TISE, the periodic boundary conditions are crucial to obtain convergence with a reasonable number of basis functions. It is not obvious how to incorporate periodic boundary conditions into a basis of moving Gaussians; 2. The most successful methods using time-evolving Gaussians use Gaussians with fixed widths. As discussed above in the context of the Coulomb

potential, Gaussians with different aspect ratios for different phase space regions may be much better suited for certain problems and it is not clear how to construct such a basis that evolves in time; 3. One can allow the active space to change in time even without letting the basis functions evolve explicitly in time. Specifically, one can introduce a time-dependent mask to tailor the active basis to those functions whose instantaneous coefficients are larger than a certain cutoff. Solving the TDSE using a time-independent basis of Gaussians has been explored by several groups [55, 59–61].

With the basis functions taken as static, the equations of motion involve the coefficients only and take the form:

$$\frac{dc_j}{dt} = -\frac{i}{\hbar} \sum_{l \in \mathcal{A}} \sum_{m \in \mathcal{A}} S^{-1} \langle \tilde{b}_l | H(t) | \tilde{b}_m \rangle c_m(t), \tag{26}$$

where $\mathcal{A}$ is the active space.

There are several possible strategies for determining a time-dependent mask. One is to use the evolution of the classical mechanical distribution as a guide for the quantum mask (this can be done in the presence of an external field as well). One would generally want to include additional functions at the boundary of the classical distribution to account for the fact that the quantum distribution may be somewhat more diffuse. A second possibility is a purely numerical algorithm: to monitor the coefficients of the basis functions at the boundary of the quantum distribution and when they grow beyond a certain threshold, to add new basis functions where they are needed. We have tested both these approaches, but more extensive tests are required to determine if one is generally to be preferred over the other.

One of our major interests is in applying the time-dependent pvb method to attosecond electron dynamics [62–65]. The time-dependent simulation of electronic systems in the presence of strong fields is very demanding computationally, especially if multiple electrons actively participate [66–70]. Ultimately, we hope to treat such systems with the time-dependent pvb method, and combine this simulation methodology with optimal control theory. For example, controlling high-order harmonic generation (HHG) is of great interest in attosecond science, not only because of the possibility of generating coherent x-rays, but also as a mechanism of generating attosecond laser pulses. The HHG process was once thought to be well-described by a single-active-electron model as pictured in Fig. 16a, but recent studies have suggested that the contributions from multi-electron dynamics can be significant [71, 72]. We intend to apply the pvb method to elucidate and exploit multi-electron mechanisms in the HHG process. Figure 16b shows another interesting challenge to which we would like to apply the pvb method: to localize multiple electrons at a particular site in a molecule by an optimally designed laser pulse. Such control may eventually allow us to alter the chemical reactivity of atomic and molecular species via ultrafast quantum electronic dynamics.

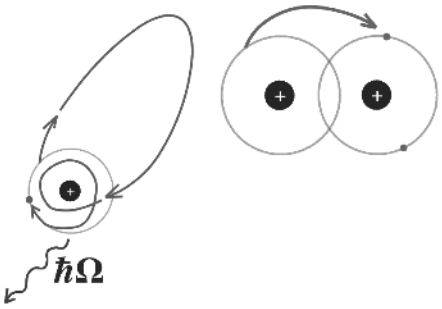

Figure 16. Schematic diagram of electron motion on the attosecond time scale. Left: Strong field ionization and recollision, leading to high harmonic generation. Right: Strong field manipulation of electronic motion in a diatomic molecule. For a color version of this figure, see the color plate section.

As a preliminary illustration of the application of the pvb method to time-dependent electronic dynamics, we solve Eq. (26) for the electronic wavepacket of a 1D atom in the combined field of near-infrared (NIR) and extreme ultraviolet (XUV) laser pulses. The Hamiltonian of this system is given as

$$H(t) = H_0 + V(t), \tag{27}$$

where H_0 is the field-free Hamiltonian with a soft-core Coulomb potential:

$$H_0 = \frac{p^2}{2\mu} - \frac{Qe^2}{4\pi\epsilon_0\sqrt{x^2 + a^2}}, \tag{28}$$

and $V(t)$ is the laser–electron coupling in the velocity gauge,

$$V(t) = -\frac{e}{\mu}[A_{\mathrm{NIR}}(t) + A_{\mathrm{XUV}}(t)]p, \tag{29}$$

where $A_{\mathrm{NIR}}(t)$ and $A_{\mathrm{XUV}}(t)$ are the vector potentials of the NIR and XUV laser pulses, respectively. The time dependence of the fields is shown in Fig. 17. For details of the parameters see Ref. [18]. Figure 18 shows the time evolution of the wavepacket in the pvb basis. It is clear that a large number of the Gaussians

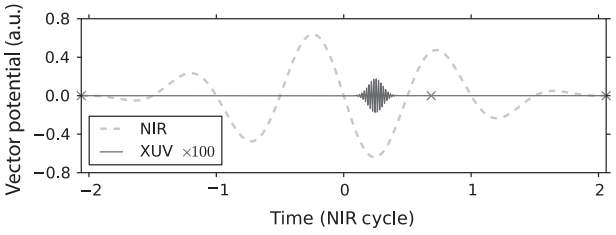

Figure 17. Vector potentials, $A_{\mathrm{NIR}}(t)$ and $A_{\mathrm{XUV}}(t)$, of the NIR and XUV laser pulses applied to the model 1D atom. For a color version of this figure, see the color plate section.

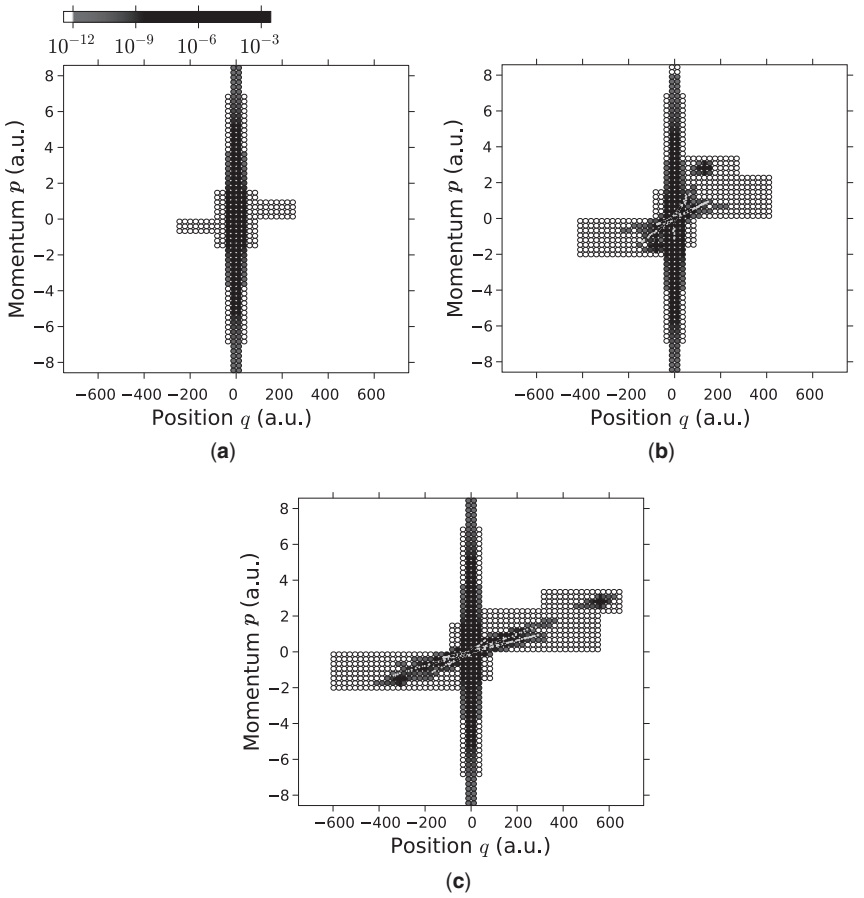

Figure 18. Snapshots of the wavepacket coefficients $\{|c_j|^2\}_{j\in\mathcal{A}}$ shown by ellipses located at the Gaussian centers $\{(q_j, p_j)\}_{j\in\mathcal{A}}$. The colors of the ellipses indicate the magnitude of $|c_j|^2$ according to the scale above the figure. The sequence of dark blue dots represent the simple-man trajectories (i.e., classical trajectories evolving in the presence of the field without the Coulomb potential) for direct ionization; the light blue dots represent the rescattered simple-man trajectories. The dark blue + marks represent the simple-man trajectories absorbing one XUV photon in the presence of the NIR field. The snapshots were taken at (a) $t = -2.06$, (b) $t = 0.69$, and (c) $t = 2.06$ in units of NIR cycles. These times are indicated by the green × marks in Fig. 17. Adapted from Ref. [18]. For a color version of this figure, see the color plate section.

have near-zero coefficients due to their negligible overlap with the wavepacket. Furthermore, it is clear that for this system the classical mechanics (shown as dots and crosses) not only provides a good guide for the quantum evolution but also provides insight into the different parts of the quantum distribution: the parts that ionized from the NIR pulse, from the XUV pulse, and the parts that underwent

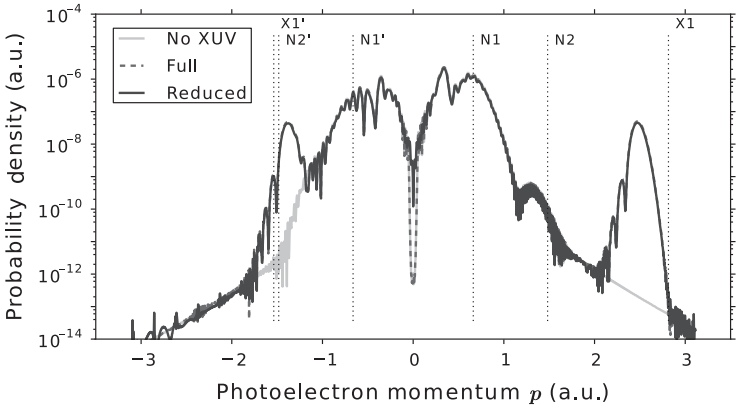

Figure 19. Comparison of the photoelectron momentum distributions obtained with the reduced pvb basis (blue solid line) and full pvb basis (red dashed line). The momentum distribution from a simulation without the XUV pulse (using the full pvb basis) is also shown (gray solid line). The vertical dashed lines indicate the cut-offs of the direct (N1 and N1′) and rescattered (N2 and N2′) photoelectrons, as well as the NIR-streaked single-XUV-photon ionization peaks (X1 and X1′), estimated by the simple-man model. Adapted from Ref. [18]. For a color version of this figure, see the color plate section.

recollision. Figure 19 shows the photoelectron distribution extracted from the wavepacket at the end of the laser pulse. The ionized part of the wavepacket was obtained by projecting out all the bound states, and the momentum distribution was calculated by projecting the ionized part on the Fourier spectral basis (i.e., plane waves). The agreement between the calculation on the full rectangular basis and on the reduced basis ($\approx 12\%$ of the functions) extends to probabilities as low as 10^{-14} (the significant deviation at $p \approx 0$ is not from an error in the dynamical calculation but in the filtering of higher lying bound states). Finally, Fig. 20 shows

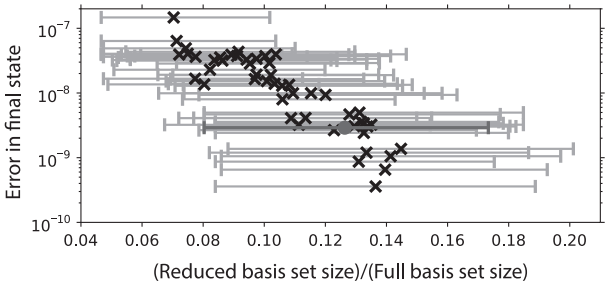

Figure 20. The error ϵ as a function of $\langle N_{\mathcal{A}} \rangle / N$ (black × marks). The horizontal error bars indicate the range of $N_{\mathcal{A}}(t)/N$ in $t_{\min} \le t \le t_{\max}$. The data marked by the red filled circle is from the simulation shown in Figs. 18 and 19. Adapted from Ref. [18]. For a color version of this figure, see the color plate section.

the error as a function of basis set size. With a basis of about 12% of the full rectangular lattice one obtains an average error of the order of 10^{-8} relative to the full rectangle.

Although this example is 1D, as discussed in the time-independent context the expected savings is expected to grow with dimension faster than $\frac{\eta^D}{D!}$. We are currently working on the application of the method to the dynamics of larger electronic systems.

V. APPLICATIONS TO AUDIO AND IMAGE PROCESSING

As discussed in the Introduction, the von Neumann basis set in x and p is isomorphic to the Gabor basis set in t and ω. It is therefore straightforward to apply the methodology described above to audio signals where the variables are t and ω, as well as to image processing, where the image is a 2D spatial signal with a conjugate variable, generally referred to as frequency, in each coordinate [19].

Figure 21 shows a "splat" signal in the time, frequency, and pgb representations. We reconstructed the signal for various basis set sizes and calculated the norm of the error (the difference between the original and the reconstructed signal). The results are shown in Fig. 22. For comparison, we show results retaining the

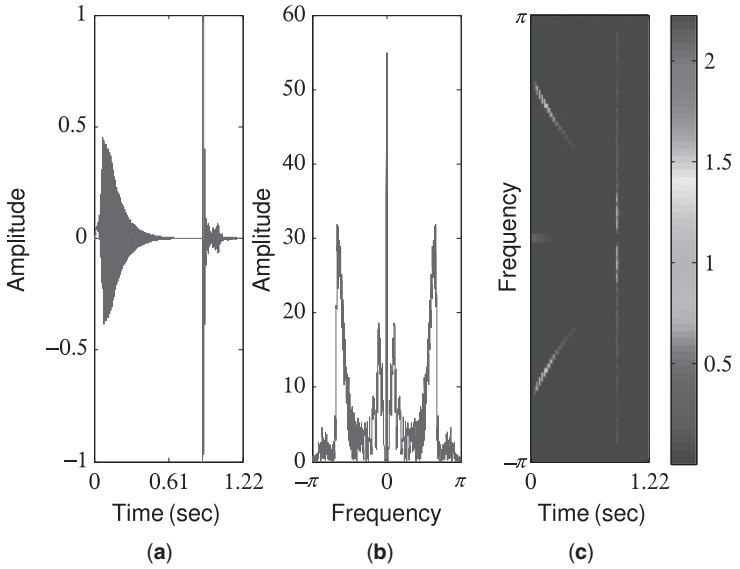

Figure 21. The splat signal in time (**a**), frequency (**b**), and pgb (**c**) representations. Adapted from Ref. [19]. For a color version of this figure, see the color plate section.

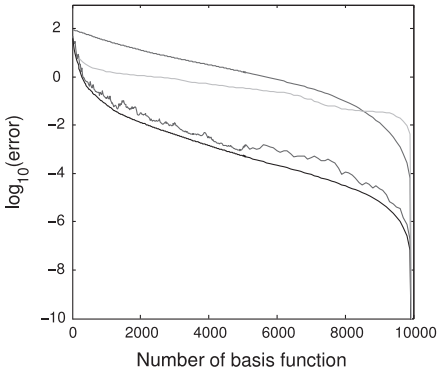

Figure 22. The norm of the error of the reconstructed signal as a function of the number of basis functions using the DFT (red), the DGE with an additional correction due to Porat (green), the pgb (blue), and the pgb with a correction developed by Porat (black). Adapted from Ref. [19]. For a color version of this figure, see the color plate section.

same number of discrete Fourier transform (DFT) coefficients. It is seen that the pgb representation gives several orders of magnitude more accuracy than the DFT for the same number of basis functions. Clearly, the pgb method allows much more compression than the DFT, but introduces some residual roughness. This roughness may be removed using an additional correction due to Porat [33], although the latter involves some additional computational cost.

A true comparison with state of the art audio compression methods will require post-processing of the pgb representation using the standard audio compression techniques, psychoacoustics, entropy coding, quantization, and non-zero mapping, which we have not yet done. It is worth noting that there is a fast Gabor transform that transforms the signal from the time to the Gabor representation and back in $\approx aN \ln N$ operations, where $1 \leq a \leq 2$ [34], potentially competitive with the FFT which scales as $N \ln N$.

We now turn to the application of the pgb method to image compression. We will demonstrate this on the Barbara image (Fig. 23a). which is a well-known benchmark for image compression. The original image contains 512×512 pixels. Figure 23 shows the reconstruction of the image using only the 20,552 largest coefficients (≈8% of the coefficients), using the discrete Gabor expansion (DGE) (b), the discrete cosine transform (DCT) (c), the DCT applied to 8×8 blocks as used in the JPEG standard (d), the Daubechies wavelet (e), and the pgb method (f). The pgb method provides an enormous improvement over the DGE, and it also has a clear advantage over the DCT. Applying the DCT on 8×8 blocks introduces correlation between spatial and frequency information, and therefore shows some of the advantages of the pgb method. However, the pgb transformation is implemented on the whole picture and therefore does not suffer from the artificial effect of blocking in the 8×8 DCT (Fig. 24). Examination of the finer details in the picture (Fig. 25) and calculating the mean square error reveal that the pgb outperforms the wavelet representation as well.

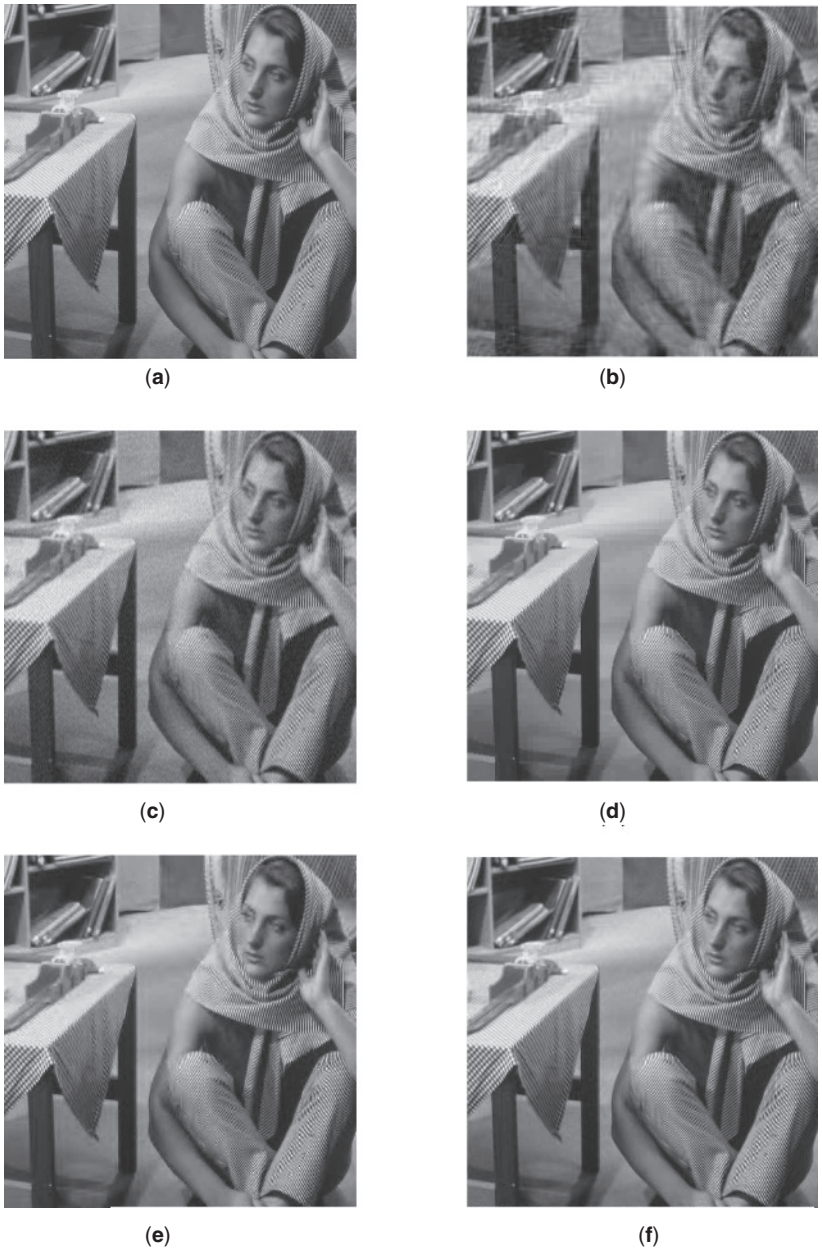

Figure 23. Reconstruction of the Barbara image using about 8% (20,552) of the coefficients. (**a**) Original picture. (**b**) DGE method. (**c**) DCT transformation. (**d**) DCT on 8 × 8 blocks. (**e**) Daubechies wavelet. (**f**) pgb method. Adapted from Ref. [19].

Figure 24. A detailed part of the original image of Fig. 23 (**a**) and the reconstructions using DCT on 8×8 blocks (**b**) and the pgb method (**c**). The artificial effect of blocking is much less severe in the pgb method. Adapted from Ref. [19].

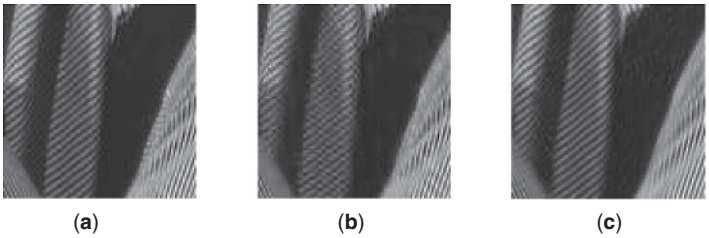

Figure 25. A detailed part of the original image of Fig. 23 (**a**) and the reconstructions using Daubechies wavelets (**b**) and the pgb method (**c**). The pgb method is seen to be much closer to the original than wavelet compression which is known to cause blurring for areas with rich sharp edges [73]. Adapted from Ref. [19].

VI. CONCLUSIONS AND FUTURE PROSPECTS

The idea of a basis of phase space Gaussians dates back to the early days of quantum mechanics. The appeal of being able to place basis functions exactly where needed in phase space has fascinated researchers in both quantum mechanics and signal processing, but in practice the approach has always suffered from convergence problems.

In this review we have discussed a simple way to converge the approach, and presented a theory that optimizes the phase space localization to obtain the most compact possible representation. We have shown applications to shaped femtosecond pulses, to the solution of time-independent and time-dependent quantum mechanical problems, and to audio and image compression.

Work in progress includes applying the method to larger quantum mechanical systems. In particular, we are currently applying the method to multidimensional electronic systems where the Coulomb singularity and the long range Coulomb attraction give rise to challenging numerical problems. We believe that the method could be useful for density functional theory (DFT) and time-dependent DFT

(TDDFT), as well as for quantum dissipative systems. In the realm of image processing, the method may have potential applications for video.

The pvb/pgb method provides an interesting case study of an approach that was developed independently in two different fields of science. Although the applications to quantum mechanics and signal processing at first glance seem very different, on deeper reflection it is clear that they have completely isomorphic underlying mathematics. Our contribution to solving the longstanding problem with the convergence of the method can be thought of metaphorically as "squaring the circle," where the Gaussian basis represents the circles and the Fourier basis the square. By "thinking inside the box" one can modify the Gaussian basis to obtain complete informational equivalence with the Fourier method. In the context of signal processing, this establishes an unexpected connection between Gabor theory, with its intuitive appeal and its promise of efficiency, and Nyquist's theorem with its rigorous error bounds. In the context of quantum mechanics it establishes an unexpected connection between two previously disparate camps: those that use Fourier (or DVR) methods and those that use Gaussian wavepacket methods. Building these unexpected connections, both within fields and between fields, is not only intellectually rewarding but potentially able to bear practical fruit, allowing new connections and techniques to be brought from one area to another.

ACKNOWLEDGMENTS

We are grateful to Tobias Brixner for a longstanding collaboration and for permission to reproduce results from our joint publications. This work was supported by the Israel Science Foundation and made possible, in part, by the historic generosity of the Harold Perlman family.

REFERENCES

1. D. Gabor, *J. Inst. Elect. Eng.* **93**, 429 (1946).
2. J. von Neumann, *Math. Ann.* **104**, 570 (1931).
3. A.M. Perelomov, *Theor. Math. Phys* **11**, 156 (1971). Technically, the Gabor lattice on the infinite plane has the peculiar property of being overcomplete by one function.
4. M.J. Davis and E. J. Heller, *J. Chem. Phys.* **71**, 3383 (1979).
5. Walter Kohn – Nobel Lecture: Electronic Structure of Matter Wave Functions and Density Functionals, Nobelprize.org. June 2, 2013. http://www.nobelprize.org/nobel_prizes/chemistry/laureates/1998/kohn-lecture.html.
6. M.J. Bastiaans, *IEEE* **68**, 538 (1980).
7. R. Balian, *C. R. Acad. Sci. III* **292**, 1357 (1981).

8. F. Low, *A Passion for Physics–Essays in Honor of Geoffrey Chew*, World Scientific, Singapore, pp. 17–22, 1985.
9. M. Porat and Y.Y. Zeevi, *IEEE Trans. Pattern Anal. Machine Intell.* **10**, 452 (1988).
10. J. Wexler and S. Raz, *Signal Process.* **21**, 207 (1990).
11. I. Daubechies, *IEEE* **36**, 961 (1990).
12. B. Poirier and A. Salam, *J. Chem. Phys.* **121**, 1690 (2004).
13. R. Lombardini and B. Poirier, *Phys. Rev. E.* **74**, 036705 (2006).
14. S. Fechner, F. Dimler, T. Brixner, G. Gerber, and D. J. Tannor, *Opt. Express* **15**, 15389 (2007).
15. F. Dimler, S. Fechner, A. Rodenberg, T. Brixner, and D. J. Tannor, *New J. Phys.* **11**, 105052 (2009).
16. A. Shimshovitz and D.J. Tannor, *Phys. Rev. Lett.* **109**, 070402 (2012).
17. A. Shimshovitz and D.J. Tannor, *J. Chem. Phys.* **137**, 101103 (2012).
18. N. Takemoto, A. Shimshovitz, and D.J. Tannor, *J. Chem. Phys.* **137**, 011102 (2012).
19. A. Shimshovitz and D.J. Tannor arXiv:1207.0632 [math:FA].
20. E.T. Whittaker, *Proc. R. Soc. Edinburgh* **35**, 181 (1915).
21. H. Nyquist, *Trans. AIEE 1* **47**, 617 (1928).
22. C.E. Shannon, *Proc. IRE* **37**, 10 (1949).
23. R. Kosloff, in: *Numerical Grid Methods and their Application to Schrödinger's Equation*, C. Cerjan, Ed., Kluwer, Boston, 1993.
24. C.C. Marston and G.G. Balint-Kurti, *J. Chem. Phys.* **6**, 3571 (1989).
25. D.T. Colbert and W. H. Miller, *J. Chem. Phys.* **96**, 1982 (1992).
26. J. Dai and J.C. Light, *J. Chem. Phys.* **107**, 1676 (1997).
27. A.J.H.M. Meijer and E.M. Goldfield, *J. Chem. Phys.* **108**, 5404 (1998).
28. X.T. Wu, A.B. McCoy, and E.F. Hayes, *J. Chem. Phys.* **110**, 2354 (1999).
29. J.H. Baraban, A.R. Beck, A.H. Steeves, J.F. Stanton, and R.W. Field, *J. Chem. Phys.* **134**, 244311 (2011).
30. D.J. Tannor, *Introduction to Quantum Mechanics: A Time-dependent Perspective*, University Science Books, Sausalito, 2007, eq. 11.163.
31. See supplementary material to [16].
32. D.J. Tannor, *Introduction to Quantum Mechanics: A Time-dependent Perspective*, University Science Books, Sausalito, 2007, eq. 8.85.
33. T. Genossar and M. Porat, *IEEE* **22**, 449 (1992).
34. R.S. Orr, *IEEE Transactions on Signal Processing* **41**, 122 (1993).
35. S. Qian and D. Chen, *IEEE Trans. Signal Proc.* **41**, 2429 (1993).
36. D.J. Tannor and S.A. Rice, *J. Chem. Phys.* **83**, 5013 (1985).
37. R. Kosloff, S.A. Rice, P. Gaspard, S. Tersigni, and D.J. Tannor, *Chem. Phys.* **139**, 201 (1989).
38. A.P. Peirce, M.A. Dahleh, and H. Rabitz, *Phys. Rev. A* **37**, 4950 (1988).
39. R.S. Judson and H. Rabitz, *Phys. Rev. Lett.* **68**, 1500 (1992).
40. A.M. Weiner, D.E. Leaird, J.S. Patel, and J.R. Wullert, *Opt. Lett.* **15**, 326 (1990).
41. A. Assion, T. Baumert, M. Bergt, T. Brixner, B. Kiefer, V. Seyfried, M. Strehle, and G. Gerber, *Science* **282**, 919 (1998).
42. E. Wigner, *Phys. Rev.* **40**, 749 (1932).
43. K. Husimi, *Proc. Phys. Math. Soc. Jpn.* **22**, 264 (1940).

44. Equation (23) (Ref. [30] Eq. 11.172), is a slightly modified version of the expression in [25] to include periodic boundary conditions.
45. A. Shimshovitz, Z. Bačić, and D.J. Tannor, in preparation.
46. Z. Bačić and J.C. Light, *Annu. Rev. Phys. Chem.* **40**, 469 (1989).
47. J.P. Modisette, P. Nordlander, J.L. Kinsey, and B.R. Johnson, *Chem. Phys. Lett.* **250**, 485 (1996); A. Maloney, J.L. Kinsey, and B.R. Johnson, *J. Chem. Phys.* **117**, 3548 (2002).
48. I.P. Hamilton and J.C. Light, *J. Chem. Phys.* **84**, 306 (1986).
49. Z. Bačić, R.M. Whitnell, D. Brown, and J.C. Light, *Comp. Phys. Comm.* **51**, 35 (1988).
50. S. Garashchuk and J.C. Light, *J. Chem. Phys.* **114**, 3929 (2001).
51. E. Fattal, R. Baer, and R. Kosloff, *Phys. Rev. E.* **53**, 1217 (1996).
52. E. J. Heller, *J. Chem. Phys.* **75**, 2923 (1981).
53. M.F. Herman and E. Kluk, *J. Chem. Phys.* **91**, 27 (1984).
54. S.I. Sawada, R. Heather, B. Jackson, and H. Metiu, *J. Chem. Phys.* **83**, 3009 (1985); S.I. Sawada and H. Metiu, *J. Chem. Phys.* **84**, 227 (1986).
55. D.V. Shalashilin and M.S. Child, *J. Chem. Phys.* **113**, 10028 (2000).
56. D.V. Shalashilin and M.S. Child, *Chem. Phys.* **304**, 103 (2004).
57. M. Ben-Nun and T.J. Martinez, *J. Chem. Phys.* **108**, 7244 (1998).
58. G.A. Worth and I. Burghardt, *Chem. Phys. Lett.* **368** 502 (2003).
59. D. Huber and E.J. Heller, *J. Chem. Phys.* **87**, 5302 (1987); ibid. **89**, 4752 (1988).
60. L.M. Andersson, *J. Chem. Phys.* **115**, 1158 (2001); L.M. Andersson, J. Åberg, H.O. Karlsson, and O. Goscinski, *J. Phys. A: Math. Gen.* **35**, 7787 (2002).
61. B. Hartke, *Phys. Chem. Chem. Phys.* **8**, 3627 (2006).
62. P.B. Corkum, *Phys. Rev. Lett.* **71**, 1994 (1993).
63. F. Krausz and M. Ivanov, *Rev. Mod. Phys.* **81**, 163 (2009).
64. I. Barth, J. Manz, Y. Shigeta, and K. Yagi, *J. Am. Chem. Soc.* **128**, 7043 (2006).
65. F. Remacle, M. Nest, and R.D. Levine, *Phys. Rev. Lett.* **99**, 183902 (2007).
66. E.S. Smyth, J.S. Parker, and K.T. Taylor, *Comp. Phys. Commun.* **114**, 1 (1998); J.S. Parker, B.J.S. Doherty, K.J. Meharg, and K.T. Taylor, *J. Phys. B Atom. Mol. Opt. Phys.* **36**, L393 (2001).
67. H.G. Muller, in: L.F. DiMauro, R.R. Freeman, K.C. Kulander, Eds., Multiphoton Processes: ICONP VIII, Proceedings of the Eighth International Conference, Melville, 2000.
68. A.S. Kheifets and I. Bray, *J. Phys. B Atom. Mol. Opt. Phys.* **31**, L447 (1998); I. Bray, D.V. Fursa, A.S. Kheifets, and A.T. Stelbovics, *J. Phys. B Atom. Mol. Opt. Phys.* **35**, R117 (2002).
69. T. Kato and H. Kono, *Chem. Phys. Lett.* **392**, 533 (2004); *J. Chem. Phys.* **128**, 184102 (2008); T. Kato and K. Yamanouchi, *J. Chem. Phys.* **131**, 164118 (2009).
70. K. Harumiya, H. Kono, Y. Fujimura, I. Kawata, and A.D. Bandrauk, *Phys. Rev. A* **66**, 043403 (2002).
71. B.K. McFarland, J.P. Farrell, P.H. Bucksbaum, and M. Guhr, *Science* **322**, 1232 (2008).
72. O. Smirnova, S. Patchkovskii, Y. Mairesse, N. Dudovich, and M.Y. Ivanov, *Proc. Nat. Acad. Sci.* **106**, 16556 (2009).
73. H. Jin, Y. You, and X. Zhou, IEEE. Symposium on Signal Processing and Its Applications, 2007.
74. R. Kosloff, *J. Phys. Chem.* **92**, 2087 (1988) and references therein.